Received: 26 December 2023 | Revised: 23 February 2024 | Accepted: 27 February 2024

DOI: 10.1002/bit.28696

ARTICLE

BIOTECHNOLOGY AND BIOENGINEERING WILEY

Residence time distribution in continuous virus filtration

Yu-Cheng Chen[1,2] | Gabriele Recanati[2] | Fernando De Mathia[2] | Dong-Qiang Lin[1] | Alois Jungbauer[2]

[1]Key Laboratory of Biomass Chemical Engineering of Ministry of Education, Zhejiang Key Laboratory of Smart Biomaterials, College of Chemical and Biological Engineering, Zhejiang University, Hangzhou, China

[2]Department of Biotechnology, University of Natural Resources and Life Sciences, Vienna, Austria

Correspondence
Alois Jungbauer, Department of Biotechnology, Muthgasse 18, Vienna 1190, Austria.
Email: alois.jungbauer@boku.ac.at

Funding information
National Key R&D Program of China, Grant/Award Number: 2021YFE0113300; Austrian Funding Agency (FFG) (Frontrunner), Grant/Award Number: 878717

Abstract

Regulatory authorities recommend using residence time distribution (RTD) to address material traceability in continuous manufacturing. Continuous virus filtration is an essential but poorly understood step in biologics manufacturing in respect to fluid dynamics and scale-up. Here we describe a model that considers nonideal mixing and film resistance for RTD prediction in continuous virus filtration, and its experimental validation using the inert tracer $NaNO_3$. The model was successfully calibrated through pulse injection experiments, yielding good agreement between model prediction and experiment ($R^2 > 0.90$). The model enabled the prediction of RTD with variations—for example, in injection volumes, flow rates, tracer concentrations, and filter surface areas—and was validated using stepwise experiments and combined stepwise and pulse injection experiments. All validation experiments achieved $R^2 > 0.97$. Notably, if the process includes a porous material—such as a porous chromatography material, ultrafilter, or virus filter—it must be considered whether the molecule size affects the RTD, as tracers with different sizes may penetrate the pore space differently. Calibration of the model with $NaNO_3$ enabled extrapolation to RTD of recombinant antibodies, which will promote significant savings in antibody consumption. This RTD model is ready for further application in end-to-end integrated continuous downstream processes, such as addressing material traceability during continuous virus filtration processes.

KEYWORDS
continuous manufacturing, downstream processing, mechanistic model, monoclonal antibody, residence time distribution, virus filtration

1 | INTRODUCTION

Virus filtration is mandatory to efficiently and robustly eliminate viral particles, without compromising product safety. Typically, virus filters are single-use devices operated under either constant pressure or constant flux conditions (Fan et al., 2021; Goodrich et al., 2020; Wickramasinghe et al., 2010). Their separation capability relies on a size-based nanofiltration membrane structure, featuring a retentive region with a pore size of 15–20 nm, that effectively captures similarly sized viral particles. On the other hand, biopharmaceuticals—such as monoclonal antibodies with dimensions of 9–12 nm—can readily pass through these membranes (Shirataki & Wickramasinghe, 2023; Suh et al., 2023).

Yu-Cheng Chen and Gabriele Recanati contributed equally to this study.

A fully end-to-end continuous biomanufacturing process must include continuous virus filtration (David et al., 2019). Research on continuous virus filtration processes is still in early stages (Bohonak et al., 2021; Fan et al., 2021; Lute et al., 2020; Shirataki et al., 2023). It is crucial to elucidate the differences between batch and continuous operations, and to master the methods for designing operation parameters of continuous processes based on batch operations. Notably, there is a significant distinction between batch and continuous operations, with regard to material traceability and understanding how disturbances propagate and affect material quality (Chen, Mao, et al., 2024; Lin et al., 2021). Regulatory authorities strongly advocate traceability in continuous manufacturing, with ICH-Q13 (2023) calling for the application of residence time distribution (RTD) to tackle this challenge. The concept of RTD originates from chemical processes, and describes the probability distribution of the time a material is present inside a reactor (Pereira & Leib, 2019). The RTD is used to determine the durations of start-up and shut-down phases, and when steady-state is achieved, and facilitates real-time control of process parameters in continuous operation.

Experimental measurement of RTD is typically achieved via tracer experiments, in which an inert material is injected into a reactor and monitored over time. However, it is not always easy to find an inert tracer that is easily detectable, inexpensive, and nontoxic, and that closely mimics the properties of the target product. Malakian et al. (2022) recently reported the use of a NaCl solution and a fluorescent dye as inert tracers to measure RTD in virus filtration processes. In another study, Lali et al. (2022) utilized a fluorescent-labeled antibody as an inert tracer in protein A affinity chromatography. If a process includes a porous material—such as a porous chromatography material, ultrafilter, or virus filter—it must be considered whether the molecule size affects the RTD, as tracers with different sizes may penetrate the pore space differently.

Mathematical models describing RTD are available for variety of reactors (Pereira & Leib, 2019). For simple standard processes, RTD can be estimated using models for continuously stirred tanks (CST), tanks in series (TIS), and dispersed plug flow (DPF), with the choice and combination depending on the extent of back-mixing in the system (Sencar, Hammerschmidt, & Jungbauer et al., 2020). Processes involving dead zones require modeling of nonideal mixing (Pancholi et al., 2022). More complex processes need more sophisticated mathematical models, and analytical solutions are not always available. These models offer greater extrapolation capabilities compared to data-driven or statistical models (Dürauer et al., 2023; Tang et al., 2023). Establishing robust and efficient models require proper model calibration and suitable calibration experiments (Chen et al., 2022; Chen, Chen, et al., 2023; Chen, Yao, et al., 2023; Yang et al., 2024). In virus filtration, pressure operations have been primarily applied and modeled, rather than considering constant flux processes (Shirataki et al., 2023, 2021). Recently, Malakian et al. (2022) developed a PF-CST-CST model to describe the RTD of virus filtration in constant flux processes. However, discrepancies are observed between the model simulations and experimental results.

Our research group has conducted extensive investigations of RTD in downstream biopharmaceutical processes (Lali et al., 2021, 2022; Sencar, Hammerschmidt, & Jungbauer et al., 2020; Sencar, Hammerschmidt, Martins, et al., 2020). However, these studies have primarily focused on either tracer experiments or model development.

In this study, our primary focus is the development and application of an RTD model for virus filtration processes. The model is ought to be robust under various perturbations, including changes in loading volumes, flow rates, tracer concentrations, and filter surface areas. First, we calibrated the RTD model by pulse injection experiments using $NaNO_3$ as a tracer. The tracer can be monitored by conductivity and UV absorbance at 280 nm, using the sensors built into the workstation. Then, we validated the model through stepwise experiments, and combined stepwise and pulse injection experiments. We also conducted tracer experiments with antibodies to confirm the suitability of $NaNO_3$ as an inexpensive replacement for antibodies, because the different sizes might affect the RTD in a virus filter. Finally, we performed a shortcut continuous virus filtration process to investigate the applicability of the RTD model calibrated under batch conditions.

2 | METHODS

2.1 | Virus filter and control system

We used Planova BioEX filters (Asahi Kasei Medical) with three distinct surface areas: 3, 10, or 100 cm^2. These dead-end filters were connected to the column valve of an ÄKTA pure 25 (Cytiva) (Figure 1). The 3-, 10-, and 100-cm^2 filters were operated at flow rates of 0.35, 1, and 10 mL/min, respectively, yielding corresponding fluxes of 70, 60, and 60 liters per square meter and hour. Before operation, all air was displaced from the filters with equilibration buffer. $UV_{280\,nm}$ and conductivity were monitored using the

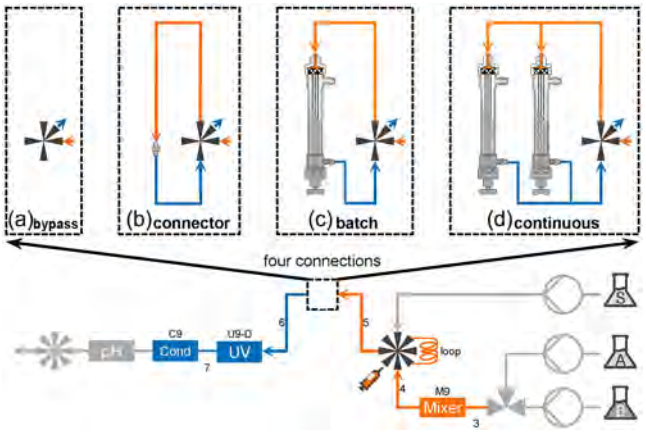

FIGURE 1 Schematic depiction of the ÄKTA system and the flow path for different experiments. (a) Bypass. (b) Experiments to measure the residence time distribution (RTD) of the chromatography workstation. (c) Experiments for batch operations with one filter. (d) Set-up for continuous operation.

integrated sensors of the ÄKTA system. Table 1 lists the manufacturer's specifications for all equipment considered for modeling.

2.2 | Mathematical models

To predict RTD characteristics of the virus filtration system, we applied several well-established RTD models. These models include not only the filtration units themselves, but also the peripheral equipment (Chen, Lu, et al., 2024), such as sample loops, tubing, valves, monitors, mixers, pumps, and the injection system. Symbols and units are provided in the Nomenclature section.

2.2.1 | Models of connections and workstation

For the workstation parts and tubing with given diameter and length —such as sample loops and tubes—we used the DPF model to calculate RTD, as follows:

$$\frac{\partial c_i}{\partial t}(z,t) = -u(t)\frac{\partial c_i}{\partial z}(z,t) + D_{ax}(t)\frac{\partial^2 c_i}{\partial z^2}(z,t), \quad (1)$$

where u and D_{ax} were obtained by $\dot{V}/A$ where $A = \pi d^2/4$, and ud/Pe where Pe was set to 0.5, respectively. The model was completed with Danckwerts boundary condition $D_{ax}(t)\frac{\partial c_i}{\partial z}(0,t) = u(t)\cdot[c_i(0,t) - c_{in,i}(t)]$ and Neumann boundary condition $\frac{\partial c_i}{\partial z}(L,t) = 0$.

For equipment, such as valves, mixer, and monitors, we used the CST model (Table 1) with $\Delta c_i = c_{in,i} - c_i$:

$$\frac{dc_i}{dt}(t) = \frac{\dot{V}(t)}{V}\Delta c_i(t). \quad (2)$$

2.2.2 | Models of virus filters

The hold-up volume of the dead-end filters can be divided into three distinct compartments: hollow spaces and headers (V_l); within the hollow fiber walls (V_{wall}), also referred to as retentate space and

TABLE 1 Description of filters and peripheral equipment in the ÄKTA system.

Label	Description	Diameter (mm)	Length (mm)	Volume (µL)	Model
3	Tubing pressure monitor to mixer	0.75	400.0	176.7	DPF
M9	Mixer	-	-	1400.0	CST
4	Tubing mixer to injection valve	0.75	200.0	88.4	DPF
Loop	Sample loop	0.5	1324.2	260.0	DPF
5	Tubing mixer to injection valve	0.75	160.0	70.7	DPF
C-VF	Tubing column valve to filter	0.75	280.0	123.7	DPF
VF-In	Inlet nozzle of filter	2.5	10.0	49.1	DPF
C	Connector	-	-	130.0	CST
VF-1-I	Hollow spaces and headers (3 cm^2)		108.0	250.9	DPF
VF-1-W	Within the hollow fiber walls (3 cm^2)	-	-	500.0	CST
VF-1-O	Permeate space (3 cm^2)	-	-	2411.6	-
VF-2-I	Hollow spaces and headers (10 cm^2)		108.0	350.9	DPF
VF-2-W	Within the hollow fiber walls (10 cm^2)	-	-	600.0	CST
VF-2-O	Permeate space (10 cm^2)	-	-	7311.6	-
VF-3-I	Hollow spaces and headers (100 cm^2)		108.0	1550.9	DPF
VF-3-W	Within the hollow fiber walls (100 cm^2)	-	-	200.0	CST
VF-3-O	Permeate space (100 cm^2)	-	-	5711.6	-
VF-Out	Inlet nozzle of filter	2.5	18.0	88.4	DPF
VF-C	Tubing filter to column valve	0.75	200.0	88.4	DPF
6	Tubing column valve to UV monitor	0.75	160.0	70.7	DPF
U9-D	UV monitor	-	-	30.0	CST
7	Tubing UV to conductivity monitors	0.75	170.0	75.1	DPF
C9	Conductivity monitor	-	-	22.0	CST

Note: Equipment label refers to the ÄKTA manual from the manufacturer
Abbreviations: CST, continuously stirred tank; DPF, dispersed plug flow.

permeate space (V_O), as illustrated in Figure 2. For each compartment, the choice of models varies based on their fluid dynamics characteristics. We made the following assumptions:

1. The fiber bundle was considered as a single hollow fiber, which was assumed to be identical among different filters.
2. The 3-cm^2 filter comprised a single fiber, while the 10- and 100-cm^2 membranes comprised unknown numbers of fibers, which were calculated using A_{10}/A_3 and A_{100}/A_3, respectively.
3. Compartment V_I was modeled as an equivalent cylinder with a uniform length (L =10.8 cm) but varying diameters ($\overline{d_j} = 2\sqrt{V_{I,j}/(\pi L)}$, $j \in \{3, 10, 100\}$). Compartments V_I and V_{wall} were characterized using the DPF and CST models, respectively.

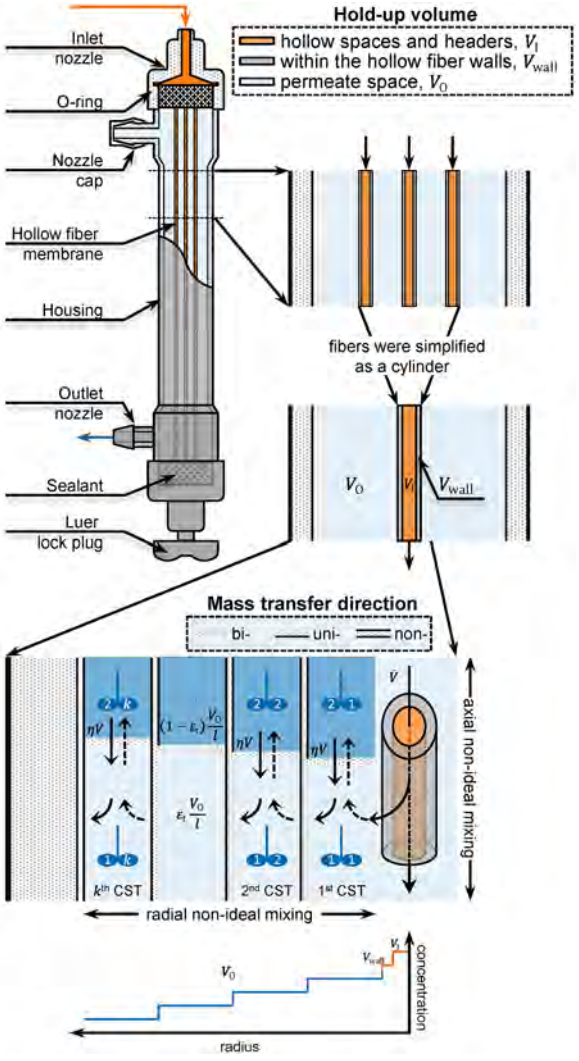

FIGURE 2 Schematic representation of virus filtration residence time distribution (RTD) models accounting for nonideal mixing and film resistance. The hold-up volume of the filters was divided into three distinct compartments V_I, V_{wall}, and V_O. The tanks in series (the number of cascaded was I) and two interconnected well-mixed CST was employed to account for the radial and axial nonideal mixing, respectively. The volumes of the two CSTs were $\varepsilon V_O/I$ and $(1-\varepsilon)V_O/I$, respectively, with an exchange of mass between the two CSTs defined as $\eta\dot{V}$.

To calculate the concentration change over time in the permeate space V_O, we developed a model that accounted for nonideal mixing in both the radial and axial directions, as well as film resistance. For radial nonideal mixing, the TIS model was employed. Permeate space V_O was divided into a cascade of CSTs arranged in an annular fashion. The concentration change of each tank was calculated using Equation (2).

For axial nonideal mixing, we used a model in which two interconnected well-mixed CSTs were divided along the axial direction (Pancholi et al., 2022). In the first axial CST, it was assumed that all solutions entered and exited. The second axial CST was assumed to have no inflow or outflow, but there was an exchange of mass between the two CSTs at a defined flow rate denoted as $\eta\dot{V}$. Consequently, the mass balance equation for the two CSTs can be derived as follows:

$$\varepsilon(t)\frac{V_O}{I}\frac{dc_i^{k1}}{dt}(t) = \dot{V}\,\Delta c_i^{k1}(t) + \eta\dot{V}\,\Delta c_i^{k2}(t), \tag{3}$$

$$[1-\varepsilon(t)]\frac{V_O}{I}\frac{dc_i^{k2}}{dt}(t) = \eta\dot{V}\,\Delta c_i^{k2}(t). \tag{4}$$

Here, the volumes of the two CSTs, $\varepsilon V_O/I$ and $(1-\varepsilon)V_O/I$, are time-dependent, and their sum equals V_O. This volume variation was explained by the flux due to film resistance. The Graetz–Leveque correlation (van den Berg et al., 1989) confirmed that the film mass transfer coefficient was proportional to $u^{1/3}$. Velocity was calculated through the side area of the equivalent cylinder, $u = \dot{V}/(\pi\overline{d_j}L)$. Thus, the flux could be defined as follows:

$$J_i(t) = u_{k1}^{1/3}(t)\cdot k_{m,i}\,\Delta c_i^{k1}(t). \tag{5}$$

The total flux contributed by all components was calculated as follows:

$$J(t) = \sum_{i=1}^{n} J_i(t). \tag{6}$$

When the concentration did not differ between the inlet and outlet materials, Δc_i^{k1} =0, signifying the absence of a second CST, where ε was equal to 1. On the other hand, when the difference was sufficient to maximize the flux, there was no first CST, such that ε was equal to 0. If we denoted the maximum flux as $k_{m,eq}\Delta c_{max}$, ε could be derived as a time-dependent linear relationship as follows:

$$1-\varepsilon(t) = \frac{A_3}{A_j}\cdot\frac{J(t)}{k_{m,eq}\Delta c_{max}}. \tag{7}$$

For a binary system comprising equilibration and tracer solutions, $\alpha = k_{m,t}/k_{m,eq}$ was defined. Combining this with Equations (5) and (6), Equation (7) can be rewritten as follows:

$$\varepsilon(t) = 1 - u_{k1}^{1/3}(t)\frac{A_3}{A_j}\frac{\Delta c_{eq}^{k1}(t) + \alpha\Delta c_t^{k1}(t)}{\Delta c_{max}}. \quad (8)$$

The domain of ε clearly fell within the range of 0–1. Therefore, we had the following equation:

$$\varepsilon(t) = \begin{cases} 1 & \varepsilon_t(t) > 1, \\ \varepsilon_t(t) & 1 \geq \varepsilon_t(t) \geq 0, \\ 0 & \varepsilon_t(t) < 0, \end{cases} \quad (9)$$

which implied that the flux contribution due to film resistance remained consistently positive, with the maximum value at Δc_{max}. Up to this point, we had obtained an RTD model for virus filtration processes, based on considerations of nonideal mixing and film resistance.

2.2.3 | Initial conditions and models of injection system

Before tracer injection, all system equipment was connected in series and flushed with low-salt buffer. Therefore, the output of the preceding equipment constituted the input for the subsequent one. For experiments involving injection via a sample loop, the loop was equilibrated using the sample itself. The salt concentration in the system before tracer injection served as the initial conditions to complete the DPF (Equation 1) and CST (Equation 2) models. Injection via pumps was represented as a rectangular pulse.

2.2.4 | Numerical solution and software

There were no available analytical solutions for these models under complex initial conditions. Therefore, numerical methods were used for their solution. For equations involving spatial variables (e.g., the DPF model), spatial discretization was achieved using the discontinuous Galerkin finite element method (Breuer et al., 2023; Meyer et al., 2020). Its semidiscrete form, along with the CST model, can be efficiently solved by SciPy (Virtanen et al., 2020) using Python 3.10. In this study, we also used several other Python packages, including NumPy (Walt et al., 2011), scikit-learn (Pedregosa et al., 2011), Pandas, and Matplotlib (Hunter, 2007).

2.2.5 | Model calibration

The developed model included four unknown parameters (l, η, α, and Δc_{max}). We used the inverse method to estimate these unknown parameters based on experimental data. If UV and conductivity signals held equal weight in the objective function, the inverse method could be formulated as an optimization problem as follows:

$$\min_{l,\eta,\alpha,\Delta c_{max}} [\Gamma^{UV}(c_h; l, \eta, \alpha, \Delta c_{max}) + \Gamma^{Cond}(c_h; l, \eta, \alpha, \Delta c_{max})]. \quad (10)$$

Computing Equation (10) required a numerical conversion of concentration units. Considering the 2-mm path length of the UV monitor, and applying Beer's law, the contribution of UV absorbance to Equation (10) is given by Equation (11):

$$\Gamma^{UV}(c_h; l, \eta, \alpha, \Delta c_{max}) = \sum_{j=1}^{m} \frac{1}{\left\| c_j^{UV} \right\|_{L^2}^2} \left\| c_j^{UV} - \sum_{i=1}^{n} \varepsilon_i L_p c_{h,i,j}(t; l, \eta, \alpha, \Delta c_{max}) \right\|_{L^2}^2. \quad (11)$$

Similarly, the contribution of conductivity could be converted using Kohlrausch's law, as follows:

$$\Gamma^{Cond}(c_h; l, \eta, \alpha, \Delta c_{max}) = \sum_{j=1}^{m} \frac{1}{\left\| c_j^{Cond} \right\|_{L^2}^2} \left\| c_j^{Cond} - \sum_{i=1}^{n} \Lambda_{m,i} c_{h,i,j}(t; l, \eta, \alpha, \Delta c_{max}) \right\|_{L^2}^2, \quad (12)$$

which was suitable for calculating strong electrolytes under ideal diluted conditions (Carta & Jungbauer, 2020). We initially used the heuristic algorithm to explore solutions for the above optimization problem over a wide range, and then applied a deterministic algorithm to obtain the final solution.

2.2.6 | Model qualification

The coefficient of determination, often referred to as R^2, indicated how well the model replicated observed outcomes. It was calculated using the r2_score function in the scikit-learn package.

2.3 | Experiments

2.3.1 | Chemicals, reagents, and protein

All chemicals and reagents were purchased from Merck or Sigma Aldrich, unless otherwise specified. Before use, all buffers were filtered using a 0.22-μm filter (Merck), and degassed in an ultrasonic bath. In this study, we used the recombinant antibody IgG1 (commercial name, trastuzumab). To prepare purified and aggregate-free antibody for virus filtration experiments, this antibody was captured via preparative protein A affinity chromatography and purified using preparative size-exclusion chromatography (details provided in the Supporting Information).

2.3.2 | Pulse injection experiments for model calibration

Pulse injection experiments were conducted as follows. First, the system was equilibrated with an equilibration buffer via pump A, until

achieving stable UV and conductivity signals. Next, 0.5 M $NaNO_3$ was loaded into a 260-μL sample loop via the ÄKTA sample pump. Finally, the sample within the sample loop was introduced into the system via pump A. The above steps were performed once for each of the three different connections: ÄKTA bypass (Figure 1a), connector (Figure 1b), and three virus filters with distinct surface areas (Figure 1c). Detailed experimental conditions are provided in Table 2 (rows C1–C3).

2.3.3 | Stepwise experiments for model validation

All experimental conditions for the stepwise experiments are outlined in Table 2 (rows V1–V4). Again, the filters were equilibrated with equilibration buffer. Subsequently, 0.05 M $NaNO_3$ was introduced directly into the system via the ÄKTA sample pump. Upon achieving a steady state, the flow was reverted to pump A. Then the same experiments were replicated using a 0.1 M $NaNO_3$. These procedures were performed using two different connections, as shown in Figure 1a (ÄKTA bypass) and Figure 1c (three virus filters with distinct surface areas).

2.3.4 | Combined stepwise and pulse injection experiments for model validation

The combined experiments resembled the stepwise experiments V1–V4, except for the inclusion of an additional sample injection during the steady state. In this step, a higher concentration sample was manually loaded into the 260-μL sample loop and introduced into the system via pump B. For experiments V5 and V6, with $NaNO_3$ used as a tracer, the sample concentrations were 0.05 and 0.5 M. In Experiment V7, antibody samples were diluted to 0.5 and 2 g/L. The above procedures were implemented in both connections, as shown in Figure 1a (ÄKTA bypass) to Figure 1c (three virus filters with distinct surface areas).

2.3.5 | Continuous virus filtration processes for model validation

A continuous virus filtration experiment, V8, was conducted to investigate whether the RTD model calibrated under batch conditions could be generalized to continuous conditions. Twin identical

TABLE 2 Summary of calibration (C) and validation (V) experiments.

No.	Sample	Experiment	Connection	Loading volume (μL)	Flow rate (mL/min)
C1	$NaNO_3$	0.5 M P	(a) ÄKTA bypass	260	1
C2–1	$NaNO_3$	0.5 M P	(b) Connector	260	0.35
C2–2	$NaNO_3$	0.5 M P	(b) Connector	260	1
C2–3	$NaNO_3$	0.5 M P	(b) Connector	260	10
C3–1	$NaNO_3$	0.5 M P	(c) 3-cm^2 filter	260	0.35
C3–2	$NaNO_3$	0.5 M P	(c) 10-cm^2 filter	260	1
C3–3	$NaNO_3$	0.5 M P	(c) 100-cm^2 filter	260	10
V1	$NaNO_3$	0.05 M S	(a) ÄKTA bypass	-	10
V2–1	$NaNO_3$	0.05 M S	(c) 3-cm^2 filter	-	0.35
V2–2	$NaNO_3$	0.05 M S	(c) 10-cm^2 filter	-	1
V2–3	$NaNO_3$	0.05 M S	(c) 100-cm^2 filter	-	10
V3	$NaNO_3$	0.1 M S	(a) ÄKTA bypass	-	10
V4–1	$NaNO_3$	0.1 M S	(c) 3-cm^2 filter	-	0.35
V4–2	$NaNO_3$	0.1 M S	(c) 10-cm^2 filter	-	1
V4-3	$NaNO_3$	0.1 M S	(c) 100-cm^2 filter	-	10
V5	$NaNO_3$	0.05 M S + 0.5 M P	(a) ÄKTA bypass	-	10
V6–1	$NaNO_3$	0.05 M S + 0.5 M P	(c) 3-cm^2 filter	-	0.35
V6–2	$NaNO_3$	0.05 M S + 0.5 M P	(c) 10-cm^2 filter	-	1
V6–3	$NaNO_3$	0.05 M S + 0.5 M P	(c) 100-cm^2 filter	-	10
V7	Antibody	0.5 g/L S + 2.0 g/L P	(c) 3-cm^2 filter	-	0.35
V8	$NaNO_3$	0.05 M continuous	(d) 100-cm^2 filter × 2	-	10

Abbreviations: P, pulse injection; S, stepwise.

100-cm^2 filters were placed at different column positions, as depicted in Figure 1d. After the first filter achieved a steady state, the column valve was switched to the next filter to simulate a continuous operation. Only two cycles were executed as a conceptual validation.

3 | RESULTS

3.1 | RTD model calibration using pulse injection experiments

First, the virus filtration RTD model was calibrated by performing pulse injection experiments, with $NaNO_3$ as a tracer. The ÄKTA bypass Experiment C1 (Figure 1a) was conducted to verify the ÄKTA dead volume. For modeling, we considered the following system equipment: the sample loop; UV monitor; conductivity monitor; and tubes 5, 6, and 7. Figure 3a shows the comparison between simulated results, generated after feeding the dead volume data into the model, and experimental results. We found that R^2 = 0.905, which indicated a good match but did not fully elucidate the RTD behavior. The experimental profiles revealed more pronounced tailing that did not fully match the simulated UV and conductivity signals. The flow rate curve indicated that the system pump required approximately a 6-s delay to reach the preset during the flow rate increase phase. These effects are dominating at very small scale and give rise to this peculiar shape.

To determine the dead volume of the tubes, we conducted pulse injection experiments, for which the filters had to be connected to the column valve. Compared to the bypass setup (Figure 1a), this configuration included the addition of C-VF and C-VF tubes, along with a connector (Figure 1b). The experimental data exhibited good agreement with the simulation, in terms of both conductivity and UV signals (Figure 3b–d). One commonly overlooked phenomenon is that at a low flow rate, the pump reached the specified flow rate with only a negligible delay, while at a high flow rate, the pulse was eluted before the specified flow rate was reached (Figure 3d). Although our model accounted for the delayed flow, Figure 3d exhibited the lowest R^2 (0.944).

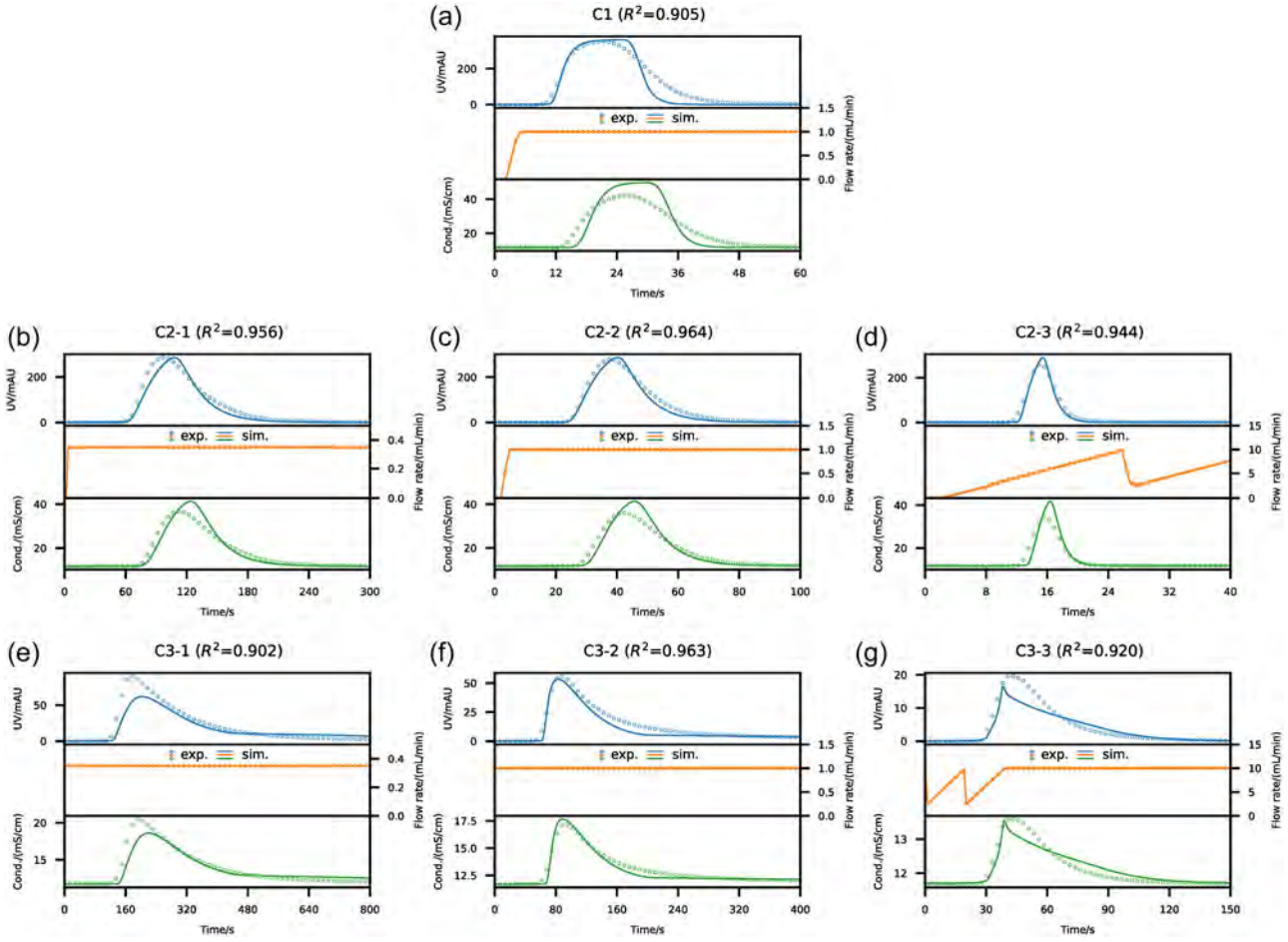

FIGURE 3 Model calibration results using a 260 µL 0.5 M NaNO3 pulse. (a) Experiment C1 (Table 2) into ÄKTA bypass at 1 mL/min; (b) experiment C2-1 (Table 2) into connector at 0.35 mL/min; (c) experiment C2-2 (Table 2) into connector at 1 mL/min; (d) experiment C2-3 (Table 2) into connector at 10 mL/min; (e) experiment C3-1 (Table 2) into 3-cm2 filter at 0.35 mL/min; (f) experiment C3-2 (Table 2) into 10-cm2 filter at 1 mL/min and (g) experiment C3-3 (Table 2) into 100-cm2 filter at 10 mL/min. The curves of the system and sample pumps were integrated.

The virus filtration RTD model was calibrated using pulse injections (Tables 2, C3–1 to C3–3) within the system where the filters were connected to the ÄKTA system (Figure 1c). Reasonable model parameters were obtained by solving the optimization problem in Equation (10), with I, η, α, and Δc_{max} values of 3, 0.13, 1.14, and 2.17E−7 M/(s/m), respectively. These parameters indicated that the RTD of permeate space could be described by three cascaded CSTs radially, with roughly 13% mass exchange between two CSTs axially, and a mass transfer ratio of 1.14 between tris-acetate and $NaNO_3$. The simulation results based on these parameters are presented in Figure 3e–g. All experimental results showed good agreement with the simulation ($R^2 > 0.9$). The filter resulted in more pronounced peak tailing, due to an increased space for exponential wash-out.

3.2 | RTD model validation using stepwise experiments

The above-described virus filtration RTD model was calibrated using pulse injection experiments with 0.5 M $NaNO_3$. To assess the extrapolation ability, we performed stepwise experiments with 0.05 and 0.1 M $NaNO_3$. The model developed for the sample loop in pulse injection experiments was not applicable to the stepwise experiments, due to the use of the ÄKTA sample pump for tracer injection.

We first conducted the bypass experiments V1 (0.05 M $NaNO_3$) and V3 (0.1 M $NaNO_3$) to demonstrate that the model could predict the stepwise injection of different $NaNO_3$ concentrations with $R^2 \approx 0.98$. Next, we performed filtration (Table 2; V2–1 to V2–3 and V4–1 to V4–3). For the 0.05 M $NaNO_3$ experiment V2 (Figure 4d–f), we observed good agreement between simulation and experiment, with $R^2 > 0.99$. For the 0.1 M $NaNO_3$ experiments V4 (Figure 4g–i), the results remained highly satisfactory, although we observed slight distinctions during the start-up and shut-down phases in the experiment using the 10-cm^2 filter. Compared to the 0.05 M $NaNO_3$ experiments, the 0.1 M $NaNO_3$ experiments required a longer time to reach a steady state, with a smooth start-up phase. In particular, the system did not fully reach a steady state in the experiments with the 10-cm^2 filter.

3.3 | RTD model validation using combined stepwise and pulse injection experiments

To emulate a process perturbation, we combined a stepwise injection with a pulse injection. We conducted combined experiments for ÄKTA bypass (Table 2, V5) and filters (Table 2, V6).

To determine whether the tracer size influenced the RTD, and whether $NaNO_3$ can be used as a surrogate for antibodies, we conducted a combined experiment (Table 2, V7) in which we loaded antibodies instead of $NaNO_3$. In the developed model, α was defined as describing the relative magnitude of mass transfer resistance between the equilibration and tracer solutions. It was assumed that α remained consistent despite the system variations. Thus, it was important to answer the following question: what $NaNO_3$ concentration is equivalent to 0.5 and 2.0 g/L antibody solutions if $c_{mAb} = \beta c_{NaNO_3}$? To address this issue, we modified the objective functions Equations (11) and (12) as follows:

$$J^{UV}(c_h;\beta) = \sum_{j=1}^{m} \frac{1}{\left\| c_j^{UV} \right\|_{L^2}^2} \left\| c_j^{UV} - \sum_{i=1}^{n} \varepsilon_i L_p c_{h,i,j}(t;\beta) \right\|_{L^2}^2, \quad (13)$$

$$J^{Cond}(c_h;\beta) = \sum_{j=1}^{m} \frac{1}{\left\| c_j^{Cond} \right\|_{L^2}^2} \left\| c_j^{Cond} - \sum_{i=1}^{n} \Lambda_{m,i} c_{h,i,j}(t;\beta) \right\|_{L^2}^2. \quad (14)$$

Solving this optimization problem yielded $\beta = 4.49$ g/M. This implied that the RTD for 0.5 and 2.0 g/L mAb solutions equaled that of 0.11 and 0.45 M $NaNO_3$, respectively. Figure 4m displays the predicted RTD in the mAb-tris-acetate system based on this equivalence relationship. We found that $R^2 = 0.99$, indicating excellent agreement between model predictions and experiments, in terms of stepwise and pulse injection.

3.4 | RTD model prediction in continuous virus filtration

Finally, the RTD model was calibrated using batch conditions and $NaNO_3$ was applied to predict continuous virus filtration of antibodies. We conducted experiment V8 using two 100-cm^2 filters connected in parallel (Figure 1d). After reaching steady state, we switched to the second filter (Figure 4n). Our results showed excellent agreement between the experiment and simulation during transitions between cycles, start-up, and shut-down, with $R^2 = 0.99$. The R^2 values for all experiments in this study are presented in Table 3 for ease of comparison.

4 | DISCUSSION

The developed RTD model was calibrated by pulse injection experiments with tracer, and was validated using three types of experiments: stepwise, a combination of stepwise and pulse injection, and continuous injection. Our results demonstrated that the model could characterize the RTD behavior of filters under six different conditions, including different injection volumes, flow rates, tracer concentrations, filter surface areas, and operating modes (e.g., continuous or batch), and with the use of $NaNO_3$ as a tracer for antibodies.

Pulse injection and stepwise injection were performed with slightly different experimental set-up, leading to varying injection volumes. Specifically, pulse injection was performed using a sample loop, while a pump was used for stepwise injection. The proposed model could predict the RTD behavior under different loading volumes (Figures 3 and 4). Our results showed a good agreement between the areas under the experimental curves and the simulated ones, indicating that the calculated results were consistent with Beer's and Kohlrausch's law.

TABLE 3 R^2 for calibration (C) and validation (V) experiments.

No.	(a) ÄKTA bypass	(b) Connector	(c) 3-cm^2 filter	(c) 10-cm^2 filter	(c) 100-cm^2 filter	(d) 100-cm^2 filter × 2
C1–C3	0.905	0.956/0.964/0/944	0.902	0.963	0.920	-
V1–V2	0.979	-	0.996	0.997	0.992	-
V3–V4	0.982	-	0.996	0.971	0.985	-
V5–V6	0.982	-	0.988	0.975	0.987	-
V7	-	-	0.990	-	-	-
V8	-	-	-	-	-	0.989

Flow rates significantly affectes the proposed RTD model. Our present study includes two types of flow rate variations. In the first type, the flow rate of the pump increases after the pump starts, which does not occur immediately, but rather with a significant delay. This phenomenon is particularly pronounced in Figure 3a,b, in which the delayed flow rate increases in a gradient pattern. In the second type, the flow rate increases in a sawtooth pattern as shown in Figures 3g,4a–c,f,i,l. All of these experiments were conducted at a higher flow rate of 10 mL/min. An explanation for this abnormal observation is that when the column valve was switched at a higher flow rate, the introduction of an additional tracer resulted in flow interruption. This overpressure phenomenon could be avoided or made negligible by reducing the flow rates. Including the flow rate change in the model enables highly accurate prediction of RTD under these complex conditions. This is because this modification can account for (a) the effects of flow rates and their impact on the axial diffusion coefficient in the DPF model, (b) the influence of flow rates in the CST model, and (c) the effects of flow rates and their impact on the mass transfer coefficient in the virus filter model.

To predict the effects of tracer concentration on RTD behavior in virus filtration processes, the DPF and CST models had to be modified. The most significant modification involves nonideal mixing, as introduced in Equations (5–7). We observed changes of the UV profile according to the sequence of buffers or tracer introduced to the system (Figure 5). This change is dependent on tracer concentration. Specifically, in validation experiments, we observed a sharper transition in the start-up phase when using 0.05 M $NaNO_3$, compared to 0.1 M $NaNO_3$. In contrast, in the shut-down phase, the transition was sharper when the higher concentration was used. We attribute this sharp transition to radial nonideal mixing, which can be characterized using the TIS model. In this model, an increased number of cascaded CSTs (l) results in altered RTD behavior, similar to in the DPF model. A single CST model and the DPF model corresponded to specific cases of the TIS model: where $l = 1$ (complete back-mixing) and where $l \rightarrow \infty$ (no back-mixing), respectively (Toson et al., 2019). The calibrated result, with $l = 3$, implies the presence of partial back-mixing in the filter. Thakur and Rathore (2021) reported a similar start-up phase phenomenon in single-pass tangential flow ultrafiltration processes, which was attributed to changes in flux induced by time-dependent membrane resistance. In our model developed for dead-end filtration, this phenomenon is explained by flux contributions from film resistance in the axial direction. Based on the contrasting RTD behavior observed in experiments using 0.05 and 0.1 M $NaNO_3$, the ratio of the film mass transfer coefficient should fall between 1 and 2. Thus, the calibrated result, $\alpha = 1.14$, is considered reasonable. In addition to the validation experiments, the 0.5 M $NaNO_3$ pulse injection experiments (Figure 3e–g) performed for model calibration also exhibited the above-described concentration-dependent phenomena, with tris-acetate displacing 0.5 M $NaNO_3$, and 0.5 M $NaNO_3$ displacing tris-acetate. This is why the simple model calibrated with pulse injection experiments can accurately predict outcomes for both stepwise experiments, and combined stepwise and pulse injection experiments. In summary, the RTD model developed based on the observations of concentration-dependent nonideal mixing provides a simple and efficient means of describing the effects of tracer concentration on the RTD behavior of filtration processes. In situations requiring a more detailed investigation of fluid flow behavior within the filter, computational fluid dynamics simulations would be a better choice (Francis et al., 2006).

The modification introduced in Equation (7), with a relative filter surface area, enables the characterization of RTD behavior for different filter surface areas in experiments C3, V2, V4, and V6. The modification simplifies all fibers as cylinders, with different diameters but equal lengths (Figure 1). It also assumes that the well-mixed volume is the same for all fibers, and equal to the volume of the simplified fiber. This assumption is simple and efficient, but ignores the interactions between fibers and assumes that the distance between fibers is much smaller than the filter diameter. Our present results confirmed that these assumptions are valid for filters with surface area in the range of 3–100 cm^2; however, their applicability to larger surfaces remains to be confirmed.

The results in Figure 4m—along with a comparison to experiments V5, V6, and V7—demonstrate the suitability of $NaNO_3$ as a tracer for monitoring antibody RTD behavior during virus filtration processes. Additionally, we obtained an equivalent relationship between their concentrations, expressed as $c_{mAb} = \beta c_{NaNO_3}$, where β =4.49 g/M. As a small-molecule tracer, the validity of this equivalence is assured under conditions characterized by minimal fouling and low membrane resistance. Considering the comprehensive factors incorporated within the developed model, this equivalence can be applied to investigate antibody RTD behavior across varying conditions, including injection volumes, flow rates, tracer

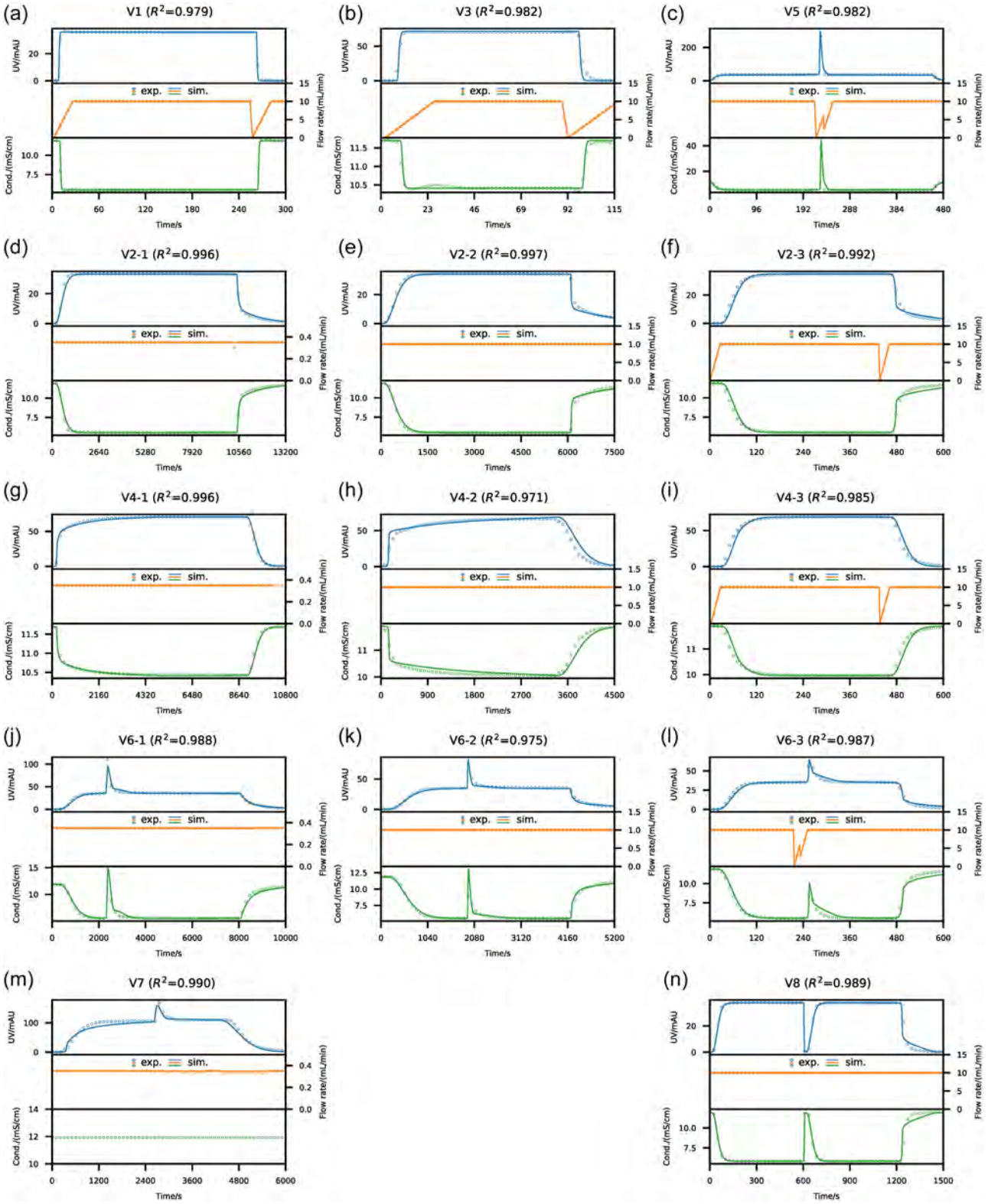

FIGURE 4 Model validation results. (a) 0.05 M NaNO3 stepwise loading; (b) 0.1 M NaNO3 stepwise loading; (c) 0.05 M NaNO3 stepwise loading with a 0.5 M NaNO3 pulse into ÄKTA bypass at 10 mL/min. 0.05 M NaNO3 stepwise loading into (d) 3-cm2 filter at 0.35 mL; (e) 10-cm2 filter at 1 mL/min; (f) 100-cm2 filter at 10 mL/min. 0.1 M NaNO3 stepwise loading into (g) 3-cm2 filter at 0.35 mL; (h) 10-cm2 filter at 1 mL/min; (i) 100-cm2 filter at 10 mL/min. 0.05 M NaNO3 stepwise loading with a 0.5 M NaNO3 pulse into (j) 3-cm2 filter at 0.35 mL; (k) 10-cm2 filter at 1 mL/min; (l) 100-cm2 filter at 10 mL/min; (m) 0.5 g/L antibody stepwise loading with a 2.0 g/L antibody pulse into 3-cm2 filter at 0.35 mL/min; (n) emulation of continuous operation by loading of 0.05 M NaNO3 on two 100-cm2 filter at 10 mL/min. The curves of the system and sample pumps were integrated.

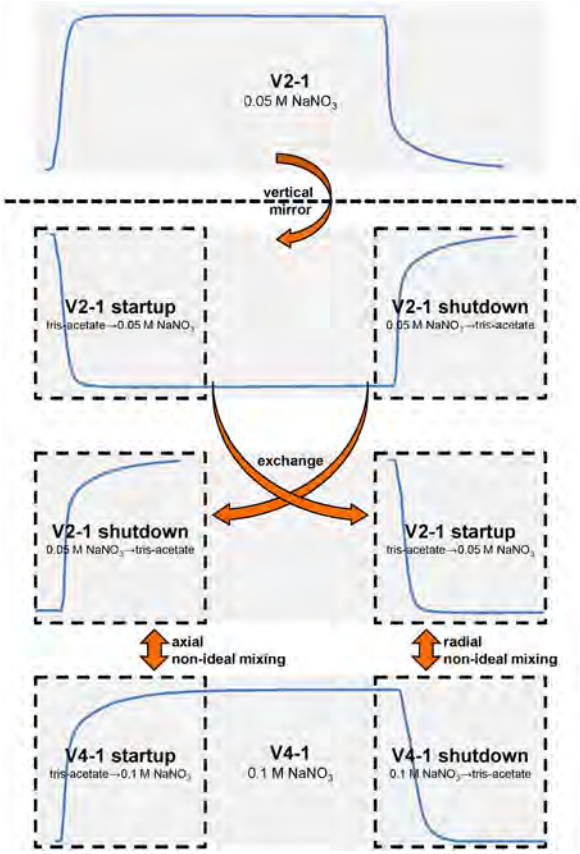

FIGURE 5 Concentration-dependent phenomena during the start-up and shut-down phases.

concentrations, filter surface areas, and operating modes. As a cost-effective tracer, $NaNO_3$ reduces antibody consumption in RTD investigation experiments, thereby reducing experimental costs. This inert tracer has significant potential for use beyond virus filtration processes into integrated continuous downstream processes of antibody production.

A good example of the proposed equivalence relationship is the use of 0.05 M $NaNO_3$ as a tracer to investigate the RTD behavior of 0.22 g/L antibodies in continuous filtration, thereby reducing the antibody consumption required for multiple cycles in continuous operation. The transition from batch to continuous conditions brings various benefits, including enhanced productivity and cost reduction. Figure 4n indicates that the continuous process with two cycles achieves approximately a 16.7% increase in productivity, compared to the batch process. A remarkable aspect of the developed model lies in its ability to describe both batch and continuous filtration processes. Based on this, there is potential for further applications of continuous virus filtration RTD models, such as in process development, optimization, characterization, and real-time control—for instance, the model-assisted steady state prediction for experimental design demonstrated in this work. Additionally, the model predicts that the productivity of the continuous process after 10 cycles will be 150% higher than that of the batch process. The ability to characterize how perturbations will affect material quality is promising for the traceability of material during the continuous virus filtration process.

5 | CONCLUSION

Here we present the development of an RTD model for the virus filtration process, which accounts for nonideal mixing and film resistance. This model was combined with CST, DPF, and TIS models, and then its estimations were compared to experimental results obtained using an ÄKTA system with three different filters with increasing areas (3/10/100 cm^2). The model was successfully calibrated by pulse injection experiments using $NaNO_3$ as a tracer, yielding $R^2 > 0.90$. The calibrated model accounts for variations—such as injection volumes, flow rates, tracer concentrations, and filter surface areas—and its excellent extrapolation capabilities were confirmed by stepwise experiments and by combined stepwise and pulse injection experiments. All validation experiments showed a good agreement between prediction and experiment, with $R^2 > 0.97$. This excellent predictive ability was attributed to the model's incorporation of nonideal mixing and film resistance. Without including film resistance we were not able to make these predictions. Moreover, the model allows extrapolation of the RTD of antibodies, even though it was calibrated using $NaNO_3$, enabling significant savings in antibody consumption. The ability to characterize how perturbations affect material quality is promising for the traceability of material during continuous virus filtration processes. In our future work, we will explore integrating virus filtration with other continuous downstream steps, such as polishing chromatography and capture processes, for the RTD modeling of an integrated downstream process.

NOMENCLATURE

A	cross sectional area [m^2]
A_j	surface area of filter j [m^2]
c_h	numerical solution [M]
c_i	outlet concentration of component i [M]
$c_{\text{in},i}$	inlet concentration of component i [M]
Δc_i	concentration difference from inlet to outlet of component i [M]
c_i^{k1}	outlet concentration of component i for k th radial and first axial CST [M]
c_i^{k2}	outlet concentration of component i for k th radial and second axial CST [M]
c_j^{Cond}	conductivity of filter j [S/m]
c_j^{UV}	UV absorbance of filter j [AU]
$\Delta c_{\max}$	flux maximum [M/(s/m)]
d	tube/fiber diameter [m]
D_{ax}	axial dispersion coefficient [m^2/s]
J	flux [M/(s/m)]
$k_{\text{m},i}$	film mass transfer coefficient of component i [−]
l	number of cascaded CSTs [−]

L	tube/fiber length [m]
L_p	path length of UV monitor [m]
m	number of filter [−]
n	number of component [−]
Pe	Peclet number [−]
t	time [s]
u	superficial velocity [m/s]
V_l	volume of hollow spaces and headers [L]
V_{wall}	volume of hollow fiber walls [L]
V_O	volume of permeate space [L]
$\dot{V}$	volumetric flow rate [L/s]
z	axial position [m]
$\|\cdot\|_{L^2}$	L^2-norm [−]

GREEK SYMBOLS

α	ratio of film mass transfer coefficient between equilibration and tracer solutions [-]
Γ	objection function [-]
ε	ratio of volume between two CSTs [-]
ε_m	extinction coefficient at 280 nm [AU/m/M]
η	ratio of flow rate between two CSTs [-]
Λ_m	molar conductivity [S/m/M]

AUTHOR CONTRIBUTION

Yu-Cheng Chen: Formal analysis; investigation; methodology; validation; visualization writing—original draft. **Gabriele Recanati**: Formal analysis; investigation; methodology; validation; visualization. **Fernando De Mathia**: Formal analysis; investigation; methodology; validation. **Dong-Qiang Lin**: Conceptualization; data curation; formal analysis; funding acquisition; writing—review and editing. **Alois Jungbauer**: Conceptualization; funding acquisition; supervision; writing—review and editing.

ACKNOWLEDGMENTS

This work was supported by a China-Austria joint project, the National Key R&D Program of China (grant no. 2021YFE0113300), and the Austrian Funding Agency (FFG) (Frontrunner; grant no. 878717). We also want to thank Shirataki Hironobu for his advice to operate Planova filters.

CONFLICT OF INTEREST STATEMENT

The authors declare no conflict of interest.

DATA AVAILABILITY STATEMENT

Data available on request from the authors

ORCID

Dong-Qiang Lin http://orcid.org/0000-0002-0504-8391
Alois Jungbauer http://orcid.org/0000-0001-8182-7728

REFERENCES

van den Berg, G. B., Rácz, I. G., & Smolders, C. A. (1989). Mass transfer coefficients in cross-flow ultrafiltration. *Journal of Membrane Science*, *47*(1), 25–51. https://doi.org/10.1016/S0376-7388(00)80858-3

Bohonak, D. M., Mehta, U., Weiss, E. R., & Voyta, G. (2021). Adapting virus filtration to enable intensified and continuous monoclonal antibody processing. *Biotechnology Progress*, *37*(2), e3088. https://doi.org/10.1002/btpr.3088

Breuer, J. M., Leweke, S., Schmölder, J., Gassner, G., & von Lieres, E. (2023). Spatial discontinuous Galerkin spectral element method for a family of chromatography models in CADET. *Computers & Chemical Engineering*, *177*, 108340. https://doi.org/10.1016/j.compchemeng.2023.108340

Carta, G., & Jungbauer, A. (2020). Introduction to protein chromatography. *Protein chromatography* (2nd ed., pp. 63–91). Wiley. https://doi.org/10.1002/9783527824045.ch2

Chen, Y.-C., Chen, X.-Y., Lin, Z.-Y., Yao, S.-J., & Lin, D.-Q. (2023). Practical teaching of modeling tools for ion-exchange chromatography: A case study. *Journal of Chemical Education*, *100*(10), 3888–3896. https://doi.org/10.1021/acs.jchemed.3c00439

Chen, Y.-C., Lu, H. L., Wang, R. Z., Sun, G., Zhang, X. Q., Liang, J. Q., Jungbauer, A., Yao, S. J., & Lin, D. Q. (2024). Standardized approach for accurate and reliable model development of ion-exchange chromatography based on parameter-by-parameter method and consideration of extra-column effects. *Biotechnology Journal*, 2300687. https://doi.org/10.1002/biot.202300687

Chen, Y.-C., Mao, R.-Q., Yao, S.-J., & Lin, D.-Q. (2024). Continuous ion-exchange chromatography for protein polishing and enrichment. In P. N. Nesterenko, C. F. Poole, & Y. Sun (Eds.), *Ion-exchange chromatography and related techniques* (pp. 535–552). Elsevier. https://doi.org/10.1016/B978-0-443-15369-3.00029-8

Chen, Y.-C., Yao, S.-J., & Lin, D.-Q. (2022). Parameter-by-parameter method for steric mass action model of ion exchange chromatography: Theoretical considerations and experimental verification. *Journal of Chromatography A*, *1680*, 463418. https://doi.org/10.1016/j.chroma.2022.463418

Chen, Y.-C., Yao, S.-J., & Lin, D.-Q. (2023). Parameter-by-parameter method for steric mass action model of ion exchange chromatography: Simplified estimation for steric shielding factor. *Journal of Chromatography A*, *1687*, 463655. https://doi.org/10.1016/j.chroma.2022.463655

David, L., Niklas, J., Budde, B., Lobedann, M., & Schembecker, G. (2019). Continuous viral filtration for the production of monoclonal antibodies. *Chemical Engineering Research and Design*, *152*, 336–347. https://doi.org/10.1016/j.cherd.2019.09.040

Dürauer, A., Jungbauer, A., & Scharl, T. (2023). Sensors and chemometrics in downstream processing. *Biotechnology and Bioengineering*, 1–18. https://doi.org/10.1002/bit.28499

Fan, R., Namila, F., Sansongko, D., Wickramasinghe, S. R., Jin, M., Kanani, D., & Qian, X. (2021). The effects of flux on the clearance of minute virus of mice during constant flux virus filtration. *Biotechnology and Bioengineering*, *118*(9), 3511–3521. https://doi.org/10.1002/bit.27778

Francis, P., Martinez, D. M., Taghipour, F., Bowen, B. D., & Haynes, C. A. (2006). Optimizing the rotor design for control led-shear affinity filtration using computational fluid dynamics. *Biotechnology and Bioengineering*, *95*(6), 1207–1217. https://doi.org/10.1002/bit.21090

Goodrich, E. M., Bohonak, D. M., Genest, P. W., & Peterson, E. (2020). Chapter 7—Recent advances in ultrafiltration and virus filtration for production of antibodies and related biotherapeutics. In A. Matte (Ed.), *Approaches to the purification, analysis and characterization of antibody-based therapeutics* (pp. 137–166). Elsevier. https://doi.org/10.1016/B978-0-08-103019-6.00007-2

Hunter, J. D. (2007). Matplotlib: A 2D graphics environment. *Computing in Science & Engineering*, *9*(3), 90–95. https://doi.org/10.1109/MCSE.2007.55

ICH-Q13. (2023). *Continuous manufacturing of drug substances and drug products*.

Lali, N., Jungbauer, A., & Satzer, P. (2021). Traceability of products and guide for batch definition in integrated continuous biomanufacturing. *Journal of Chemical Technology & Biotechnology*, *97*(9), 2386–2392. https://doi.org/10.1002/jctb.6953

Lali, N., Satzer, P., & Jungbauer, A. (2022). Residence time distribution in counter-current protein A affinity chromatography using an inert tracer. *Journal of Chromatography A*, *1683*, 463530. https://doi.org/10.1016/j.chroma.2022.463530

Lin, D.-Q., Zhang, Q.-L., & Yao, S.-J. (2021). Model-assisted approaches for continuous chromatography: Current situation and challenges. *Journal of Chromatography A*, *1637*, 461855. https://doi.org/10.1016/j.chroma.2020.461855

Lute, S., Kozaili, J., Johnson, S., Kobayashi, K., & Strauss, D. (2020). Development of small-scale models to understand the impact of continuous downstream bioprocessing on integrated virus filtration. *Biotechnology Progress*, *36*(3), e2962. https://doi.org/10.1002/btpr.2962

Malakian, A., Jung, S. Y., Afzal, M. A., Carbrello, C., Giglia, S., Johnson, M., Miller, C., Rayfield, W., Boenitz, D., Cetlin, D., & Zydney, A. L. (2022). Development of a transient inline spiking system for evaluating virus clearance in continuous bioprocessing—Proof of concept for virus filtration. *Biotechnology and Bioengineering*, *119*(8), 2134–2141. https://doi.org/10.1002/bit.28119

Meyer, K., Leweke, S., von Lieres, E., Huusom, J. K., & Abildskov, J. (2020). ChromaTech: A discontinuous Galerkin spectral element simulator for preparative liquid chromatography. *Computers & Chemical Engineering*, *141*(2), 107012. https://doi.org/10.1016/j.compchemeng.2020.107012

Pancholi, K. C., Sen, N., Singh, K. K., Vincent, T., & Kaushik, C. P. (2022). Transient heat transfer during startup of a thermal plasma chamber: Numerical insights. *Progress in Nuclear Energy*, *152*, 104371. https://doi.org/10.1016/j.pnucene.2022.104371

Pedregosa, F., Varoquaux, G., Gramfort, A., Michel, V., Thirion, B., Grisel, O., Blondel, M., Prettenhofer, P., Weiss, R., Dubourg, V., Vanderplas, J., Passos, A., Cournapeau, D., Brucher, M., Perrot, M., & Duchesnay, E. (2011). Scikit-learn: Machine learning in Python. *Journal of Machine Learning Research*, *12*, 2825–2830. https://doi.org/10.48550/arXiv.1201.0490

Pereira, C. J., & Leib, T. (2019). Section 19. Reactors. In D. W. Green, & M. Z. Southard (Eds.), *Perry's chemical engineers' handbook* (9th ed.). Mac Graw Hill.

Sencar, J., Hammerschmidt, N., & Jungbauer, A. (2020). Modeling the residence time distribution of integrated continuous bioprocesses. *Biotechnology Journal*, *15*(8), 2000008. https://doi.org/10.1002/biot.202000008

Senčar, J., Hammerschmidt, N., Martins, D. L., & Jungbauer, A. (2020). A narrow residence time incubation reactor for continuous virus inactivation based on packed beds. *New Biotechnology*, *55*, 98–107. https://doi.org/10.1016/j.nbt.2019.10.006

Shirataki, H., Matsumoto, Y., Konoike, F., & Yamamoto, S. (2023). Viral clearance in end-to-end integrated continuous process for mAb purification: Total flow-through integrated polishing on two columns connected to virus filtration. *Biotechnology and Bioengineering*, *120*(10), 2977–2988. https://doi.org/10.1002/bit.28464

Shirataki, H., & Wickramasinghe, S. R. (2023). Predicting virus filter performance using an advanced membrane structural model. *Journal of Membrane Science*, *685*, 121929. https://doi.org/10.1016/j.memsci.2023.121929

Shirataki, H., Yokoyama, Y., Taniguchi, H., & Azeyanagi, M. (2021). Analysis of filtration behavior using integrated column chromatography followed by virus filtration. *Biotechnology and Bioengineering*, *118*(9), 3569–3580. https://doi.org/10.1002/bit.27840

Suh, D., Jin, H., Park, H., Lee, C., Cho, Y. H., & Baek, Y. (2023). Effect of protein fouling on filtrate flux and virus breakthrough behaviors during virus filtration process. *Biotechnology and Bioengineering*, *120*(7), 1891–1901. https://doi.org/10.1002/bit.28407

Tang, S.-Y., Yuan, Y.-H., Chen, Y.-C., Yao, S.-J., Wang, Y., & Lin, D.-Q. (2023). Physics-informed neural networks to solve lumped kinetic model for chromatography process. *Journal of Chromatography A*, *1708*, 464346. https://doi.org/10.1016/j.chroma.2023.464346

Thakur, G., & Rathore, A. S. (2021). Modelling and optimization of single-pass tangential flow ultrafiltration for continuous manufacturing of monoclonal antibodies. *Separation and Purification Technology*, *276*(1), 119341. https://doi.org/10.1016/j.seppur.2021.119341

Toson, P., Doshi, P., & Jajcevic, D. (2019). Explicit residence time distribution of a generalised cascade of continuous stirred tank reactors for a description of short recirculation time (bypassing). *Processes*, *7*(9), 615. https://doi.org/10.3390/pr7090615

Virtanen, P., Gommers, R., Oliphant, T. E., Haberland, M., Reddy, T., Cournapeau, D., Burovski, E., Peterson, P., Weckesser, W., Bright, J., van der Walt, S. J., Brett, M., Wilson, J., Millman, K. J., Mayorov, N., Nelson, A. R. J., Jones, E., Kern, R., Larson, E., … Vázquez-Baeza, Y. (2020). SciPy 1.0: Fundamental algorithms for scientific computing in Python. *Nature Methods*, *17*(3), 261–272. https://doi.org/10.1038/s41592-019-0686-2

Walt, S. vd, Colbert, S. C., & Varoquaux, G. (2011). The NumPy array: A structure for efficient numerical computation. *Computing in Science & Engineering*, *13*(2), 22–30. https://doi.org/10.1109/MCSE.2011.37

Wickramasinghe, S. R., Stump, E. D., Grzenia, D. L., Husson, S. M., & Pellegrino, J. (2010). Understanding virus filtration membrane performance. *Journal of Membrane Science*, *365*(1), 160–169. https://doi.org/10.1016/j.memsci.2010.09.002

Yang, Y.-X., Chen, Y.-C., Yao, S.-J., & Lin, D.-Q. (2024). Parameter-by-parameter estimation method for adsorption isotherm in hydrophobic interaction chromatography. *Journal of Chromatography A*, *1716*, 464638. https://doi.org/10.1016/j.chroma.2024.464638

How to cite this article: Chen, Y.-C., Recanati, G., De Mathia, F., Lin, D.-Q., & Jungbauer, A. (2024). Residence time distribution in continuous virus filtration. *Biotechnology and Bioengineering*, *121*, 1876–1888. https://doi.org/10.1002/bit.28696